

# Stress Distributions in Plasma-Sprayed Thermal Barrier Coatings Under Thermal Cycling in a Temperature Gradient

**Andi M. Limarga**

School of Engineering and Applied Sciences,  
Harvard University,  
Cambridge, MA 02138  
e-mail: limarga@seas.harvard.edu

**Robert Vaßen**

Institut für Werkstoffe und Verfahren der  
Energietechnik 1,  
Forschungszentrum Jülich GmbH,  
52425 Jülich, Germany

**David R. Clarke**

School of Engineering and Applied Sciences,  
Harvard University,  
Cambridge, MA 02138

*The residual stress distribution in plasma-sprayed zirconia thermal barrier coatings subjected to cyclic thermal gradient testing was evaluated using Raman piezospectroscopy and finite element computation. The thermal gradient testing (approximately 440°C/mm at temperature), consisted of repeated front-side heating with a flame and constant cooling of the back-side of the substrate either with front-side radiative cooling only or with additional forced air cooling between the heating cycles. The coatings exhibited characteristic “mud-cracking” with the average crack spacing dependent on the cooling treatment. This is consistent with finite element calculations and Raman spectroscopy measurements in which the sudden drop in coating surface temperature on initial cooling leads to a large biaxial tension at the surface. The key to proper interpretation of the Raman shifts is that the stress-free Raman peaks need to be corrected for shifts associated with the evolution of the metastable tetragonal phase with aging.*

[DOI: 10.1115/1.4002209]

*Keywords: thermal barrier coating, Raman piezospectroscopy, residual stress, thermal gradient*

## 1 Introduction

The primary functional role of thermal barrier coatings (TBCs) is to enable the gas temperature ( $T_4$ ) in the hottest portion of turbines to be substantially higher than the maximum surface temperature of the bare metallic blades and vanes would otherwise allow [1,2]. This is achieved by internal cooling of the blades and vanes with the outer surface of the thermal barrier coatings being exposed to the hot gases. The TBC provides the thermal insulation and so, consequently, thermal barrier coatings are always used in a temperature gradient.

While substantial progress has been made in identifying failure modes under isothermal cyclic tests in which there is no temperature gradient, and relating the modes to various properties of the TBC and underlying bond-coat alloys [3–6], there remains a paucity of knowledge of failure mechanisms under cyclic thermal gradient conditions. Because the thermal gradients can be large in engines, cyclic thermal gradient experiment is generally performed in burner rigs. Transient stresses are also more complicated under cyclic temperature gradient tests since the stresses vary with position as well as temperature in the coating [7], so greater reliance has to be placed on finite element calculations of the temperature and stress distributions. To validate the predictions of the calculations, high-resolution measurements of the stresses in the coating are needed.

Unfortunately, the measurement of stresses in coatings has not been well established and the majority of techniques that have been applied, namely, X-ray diffraction [8,9], neutron diffraction [10,11], curvature measurement [12,13], and layer-by-layer removal method [13,14] provide an average stress in the coating and are not able to reveal the stress distribution through the coating. High spatial resolution X-ray diffraction using intense long wavelength X-rays, such as those at synchrotrons, offer considerable

potential but the application of these methods to actual components is rather difficult or, in some cases, impractical. For this reason, a number of groups have used Raman piezospectroscopy since it offers a significant advantage in that it can be localized by using a focused laser probe and, hence, can be used to resolve the stress distribution in the coating due to its high spatial resolution (of the order of 1  $\mu\text{m}$ ). Although these have been performed at room temperature, they can also be carried out at high temperature (HT) with appropriate instrumentation. However, there is reason to doubt the actual numerical values of the stresses reported since it has been assumed that the stress-free lattice parameters of zirconia are constant, irrespective of the length of time and temperature that the zirconia has been exposed to. The difficulty arises because the majority of current thermal barrier coatings are made of the metastable tetragonal phase of yttria-stabilized zirconia. Over prolonged, high-temperature exposure, the yttria ions partition by diffusion in the metastable phase to produce a two-phase mixture of equilibrium tetragonal and cubic phases, each with its own lattice parameter [15]. Thus, the stress-free lattice parameter varies with aging. Taken together with the variation in temperature through a coating in a gradient, this further complicates the derivation of the stress distribution. As will be shown in this work, this affects the values of the stresses derived from the measurements.

In this contribution, we discuss the effect of cooling rate on the stresses developed in plasma-sprayed coatings subject to cyclic testing in a thermal gradient. The stresses are evaluated using finite element analysis and compared with those calculated analytically [7]. In addition, Raman piezospectroscopy was used to quantify the residual stresses after cooling to room temperature and compared with those calculated by finite element analysis. These are then related to the “mud-cracking” observed in the coatings after thermal cycling. This paper seeks to: (i) obtain an understanding on how the cooling scenario influences the stress in coatings and in turn, the causes of the observed cracking and (ii)

Contributed by the Applied Mechanics of ASME for publication in the JOURNAL OF APPLIED MECHANICS. Manuscript received December 11, 2009; final manuscript received July 8, 2010; accepted manuscript posted July 23, 2010; published online October 8, 2010. Assoc. Editor: Thomas W. Sheild.

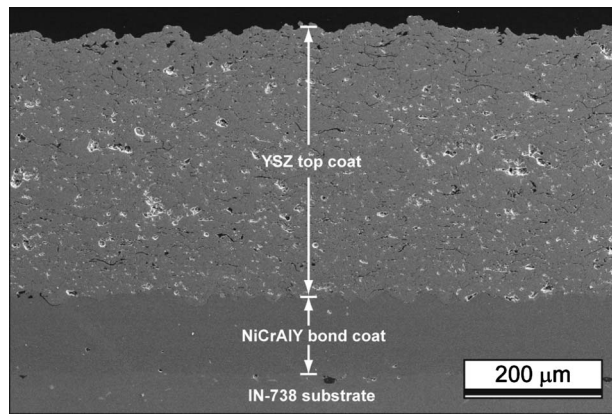


**Fig. 1 Cross-sectional micrograph of the plasma-sprayed thermal barrier coating in its as-sprayed condition**

present a rigorous methodology of applying Raman piezospectroscopy to determine the residual stress distributions in thermal barrier coatings.

## 2 Experimental Details

**2.1 Specimen and Thermal Cycling Setup.** The material investigated consisted of an IN-738 nickel-based superalloy substrate (3 mm thick, 30 mm diameter) coated with 150 μm thick NiCoCrAlY bond coat deposited using vacuum plasma spray and a 500 μm thick air plasma-sprayed top coat of 8 wt % yttria-stabilized zirconia (8YSZ). The coatings were applied at FZ Jülich (IEF-1). The substrates were grit-blasted prior to deposition and the specimens were heat treated afterwards to improve the coating adhesion. A typical microstructure of the coating in its as-sprayed condition is shown in Fig. 1.

Cyclic thermal gradient experiments were performed at FZ Jülich using an experimental setup shown in Fig. 2 and described in detail elsewhere [16]. The temperature of the TBC outer surface was measured with an infrared pyrometer operating at 8–11.5 μm while the temperature in the middle of the metallic substrate thickness was measured using a K-type thermocouple. The thermal cycle used consisted of a 5 min heating period with approximately 4 min high-temperature hold followed by a 2 min cooling periods (Fig. 3). During the heating and holding periods, the front side of the specimen (the top of the TBC) was heated using a natural gas/oxygen burner while the backside was cooled with compressed air. At the end of the high-temperature hold, the burner was rapidly moved away from the specimen while the cooling of the backside was continued. A total of 400 cycles was

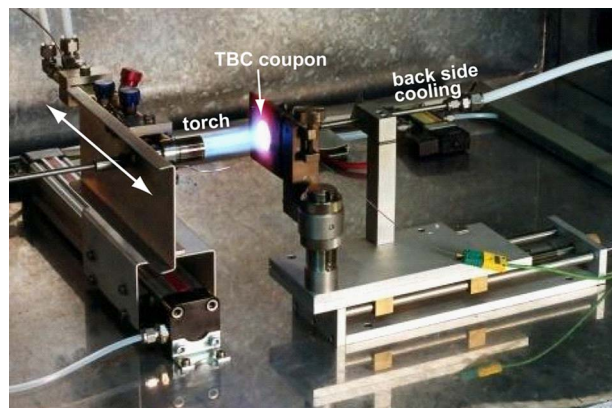


**Fig. 2 Experimental setup of the cyclic thermal gradient experiment**

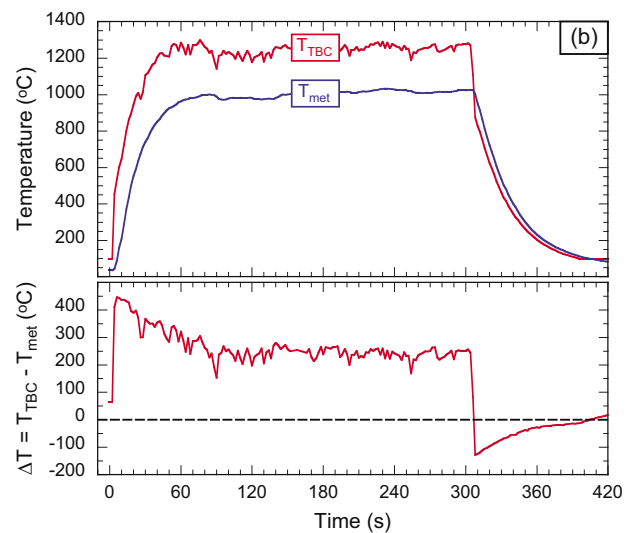
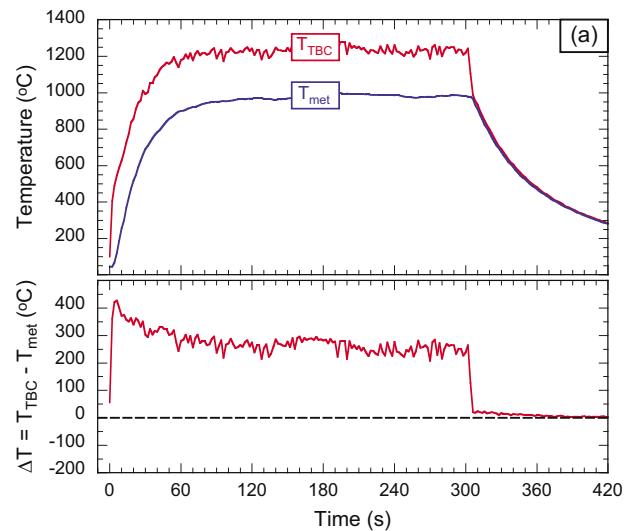


**Fig. 3 Measured temperatures of the metal and the coating surface during thermal gradient cycling: (a) with back-side cooling and (b) with front-side cooling with compressed air. The bottom panel shows the temperature difference between the coating and the metal.**

performed on the specimens before they were removed from the thermal cycling rig. In another set of experiment, an identical cyclic thermal gradient was performed for 399 cycles. In the last cycle (cycle #400), the front-side cooling was augmented using compressed air. This treatment resulted in a different cooling scenario, one in which the surface of the TBC cools faster than the interior (Fig. 3).

**2.2 Raman Spectroscopy.** Raman spectra were recorded on cross sections cut of the specimens after they were mounted in epoxy to ensure that the coating remained intact. The measurements were made using 633 nm laser excitation in a confocal Raman microprobe (LabRAM Aramis, Horiba Jobin Yvon, Edison, NJ). Raman spectra were acquired as a function of distance in the cross sections from the outer surface of the TBC and the results reported in this study were the average and standard deviation from ten different locations at the same distance from the top surface. The peak positions of each spectrum were then obtained through a deconvolution procedure using commercial peak-fitting software (GRAMS, Thermo Electron Corp., Philadelphia, PA) assuming mixed Lorentzian and Gaussian profiles for Raman lines at 465 cm<sup>-1</sup>, 610 cm<sup>-1</sup>, and 640 cm<sup>-1</sup>. The other characteristic

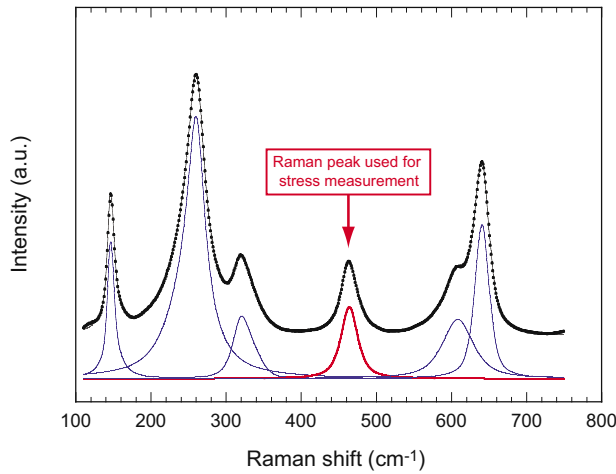


**Fig. 4 Typical Raman spectrum and peak-fitting results from tetragonal zirconia. Residual stress in the coating is determined by evaluating the shift of Raman peak at 465 cm<sup>-1</sup>.**

Raman lines of tetragonal zirconia at 145 cm<sup>-1</sup>, 260 cm<sup>-1</sup>, and 320 cm<sup>-1</sup> are asymmetric and, hence, fitted using Breit–Wigner profile (an asymmetric Lorentzian function) [15] using ORIGINPRO package (OriginLab Corp., Northampton, MA). A typical example of this curve-fitting procedure is shown in Fig. 4 with the deconvoluted peaks also indicated. In previous Raman piezospectroscopy measurements of residual stress distribution in tetragonal-zirconia thermal barrier coatings, the shift of the Raman peak at around 640 cm<sup>-1</sup> was used since it has a good signal to noise ratio [13,17–19]. However, our recent study on piezospectroscopy of tetragonal zirconia indicated that the peak at 465 cm<sup>-1</sup> is more suitable for stress measurement due to its larger piezospectroscopic constant, making it more sensitive to stress [20]. Furthermore, this peak is well isolated from the other Raman peaks, resulting in a smaller uncertainty in the curve-fitting process and, hence, more precise determination of the peak frequency.

To correct for possible shifts of the stress-free position of the Raman peak due to the evolution of the metastable phase with time at temperature, small pieces of as-sprayed coating (approximately 2 mm<sup>2</sup> in area) were scraped off and each annealed in air at different temperatures for 27 h. The temperatures selected, from 1050°C up to 1350°C, were to replicate the temperatures at various locations in the coating during thermal cycling while the duration of the annealing corresponded to the total accumulated time of the coating at temperature during thermal cycling.

**2.3 Raman Piezospectroscopy.** The evaluation of stresses by Raman piezospectroscopy relies on the measurement of the shift of Raman lines relative to their unstrained state. In the linear elastic regime, the change in frequency,  $\Delta\nu$  is related to the stress tensor by the relationship

$$\Delta\nu = \nu - \nu_0 = \Pi_{ij}\sigma_{ij} \quad (1)$$

where  $\Delta\nu$  refers to the frequency shift from the stress-free state ( $\nu_0$ ),  $\Pi_{ij}$  is the piezospectroscopic (PS) tensor, and  $\sigma_{ij}$  is the stress tensor (suffixes are written according to the repeated index notation). In polycrystalline materials with no crystallographic texture, Eq. (1) reduces to the simpler form

$$\Delta\nu = \Pi\langle\sigma\rangle \quad (2)$$

where  $\Pi$  and  $\langle\sigma\rangle$  are the trace of the PS constants and the spatial average stress tensor, respectively. Strictly speaking, the Raman peak shift is influenced by the strain (rather than stress) in the material. The piezospectroscopic constant for dense tetragonal-zirconia was measured under uniaxial stress and it was found to

be 2.01 cm<sup>-1</sup>/GPa for the Raman peak at 465 cm<sup>-1</sup> [20]. To obtain the strain distribution in the coating, the stress-based PS constant can be converted to strain-based constant with a simple relationship.

$$\Pi(\varepsilon) = \frac{E}{1 - 2\nu_n}\Pi(\sigma) \quad (3)$$

where  $\Pi(\varepsilon)$  and  $\Pi(\sigma)$  are strain-based and stress-based PS constants, respectively.  $E$  and  $\nu_n$  are the elastic modulus and Poisson's ratio of the material, respectively. Assuming  $E=200$  GPa and  $\nu=0.2$  for dense zirconia, the strain-based PS constant,  $\Pi(\varepsilon)$  is 670 cm<sup>-1</sup> (per unit strain). It is emphasized that the strain calculated from Raman peak shift refers to the trace of strain tensor  $\varepsilon_{ii}=(\varepsilon_{11}+\varepsilon_{22}+\varepsilon_{33})$ .

### 3 Finite Element Calculations

To evaluate the temperature and thermal stress distribution within the coating during thermal cycling with a temperature gradient, finite element analysis was performed using the ABAQUS code (Simulia, Providence, RI). An axisymmetric model used in the analysis represents the thermal barrier coated superalloys with identical geometry and dimension mentioned above. For simplicity, all interfaces (TBC/bond coat, bond coat/thermally grown oxide (TGO), and TGO/superalloys) were assumed to be flat and have perfect bonding. Furthermore, stress relaxation due to cracking was not taken into consideration. However, creep processes and plasticity (particularly at high temperature) were included in the analysis. The temperature-dependent material properties used in the finite element simulation were obtained from Refs. [21–26] and are listed in Table 1. Pertinent to comparison with Raman spectroscopy, the elastic modulus of plasma-sprayed zirconia was assumed to be 50 GPa. The creep behavior of the bond coat, TGO and the TBC layer was assumed to follow a Norton power-law equation  $\dot{\varepsilon}=A\sigma^n \exp(-Q/RT)$  and their parameters were listed in Table 2.

Heating and cooling were simulated by applying heat convection as the boundary conditions on the TBC surface and the backside of the metal. In the calculations, the convection coefficients and gas temperature were adjusted so that the simulated thermal history matched the measurements of the difference in temperature between the TBC surface and the midpoint of the superalloy substrate (Fig. 5). As the thermal properties of the substrate and the coating have previously been well characterized, the agreement between the calculated time-dependent temperature distribution and the measured temperatures was considered sufficient to describe the temperature distribution in the system during cyclic thermal gradient testing. Our finite element analysis using these material properties indicated that the stress distribution does not change with the number of thermal cycles that the samples were subjected to and that the accumulated stresses in previous cycles were completely relaxed prior to cooling. This is also the assumption made by Evans and Hutchinson [7] in their analysis. For these reasons, only the effects of cooling rate on the distribution of stresses during the last thermal cycle are presented here.

## 4 Results

**4.1 Microstructural Observation on TBC Surface Cracking.** The observation on the surface of the TBC after planarizing by polishing showed that the coatings all developed a network of surface cracks, commonly referred to as mud-cracking (Fig. 6). These cracks are not visible without first polishing the top of the coating to remove its roughness. The crack spacing varies from 500  $\mu\text{m}$  in the coating cooled from the backside down to 100–250  $\mu\text{m}$  in the coating cooled from both sides. The presence of cracks perpendicular to the coating surface/interface indicated that the coating surface had been subjected to a large in-plane tensile stress [7] during the tests. The origin of the stresses is described in the following section.

**Table 1 Material properties used in finite element simulation [21–26]**

Material	T (°C)	E (GPa)	$\nu$	Yield strength (MPa)	Density (kg/m <sup>3</sup> )	CTE (ppm/°C)	Thermal conductivity (W/m K)	Specific heat (J/kg K)
IN-738	25	202	0.3	953	8500	11.44	8.72	428
	650	165		817		14.44	19.66	594
	800	156		789		15.16	22.28	636
	900	150		555		15.64	24.03	675
	1000	144		344		16.12	25.78	727
NiCoCrAlY	25	152	0.3	868	7320	12.59		
	500	136		807		14.33	21	628
	600	133		562		14.97		
	700	128		321		15.64		
	800	117		191		16.30		
	900	100		92		16.94	24	674
	1000	74		52		17.51		
	1100	41				17.99	34	712
TGO	25	360	0.25		3970	8.00	20.00	790
	1000			100				
	1300			100				
8YSZ	25	50	0.25		5100	10.00	0.70	479
	500					9.64	0.70	445
	1000					10.34	0.70	445

**Table 2 Creep properties of materials [21,25,26]**

Material	A (s <sup>-1</sup> MPa <sup>-n</sup> )	Q (kJ/mol)	n
NiCoCrAlY	10 <sup>12</sup>	500	3
TGO	6.8 × 10 <sup>3</sup>	424	1
8YSZ	10 <sup>10</sup>	625	4

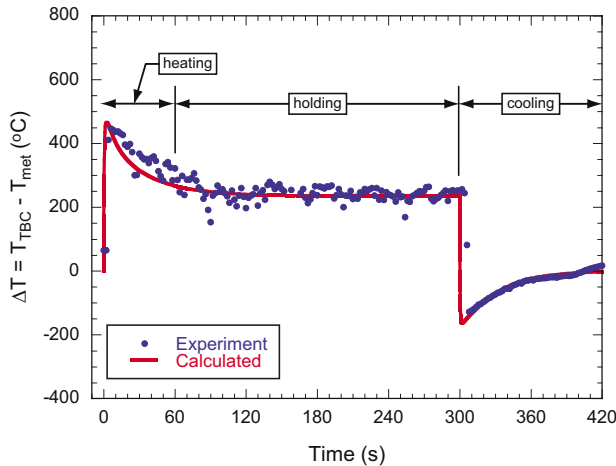
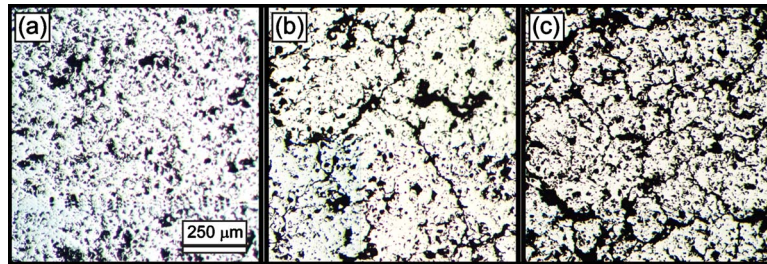


**Fig. 5 Temperature difference between the metal and the coating surface measured during experiment with front-side cooling and calculated using finite element analysis**

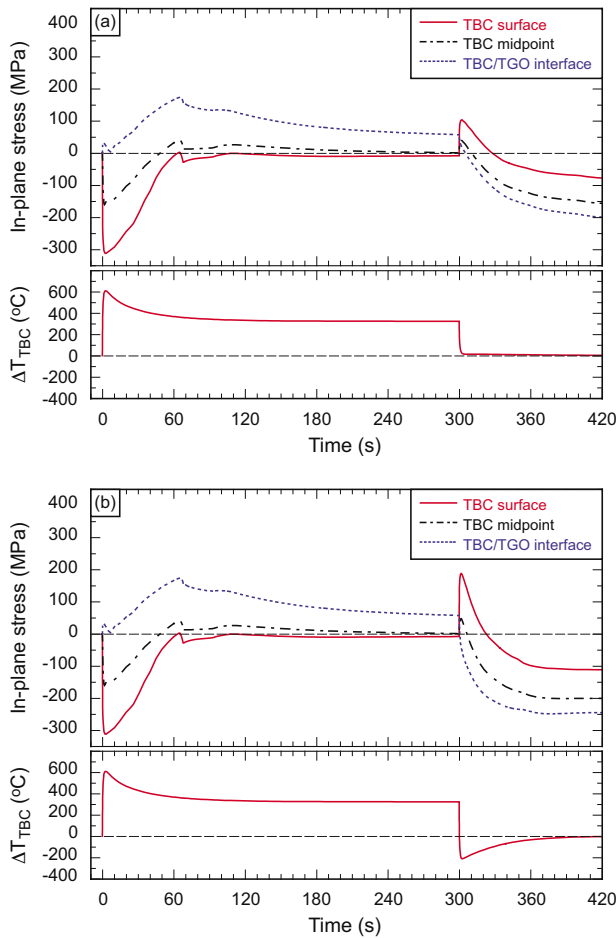
**4.2 Finite Element Analysis of the Stress Evolution in the Coating.**

Figure 7 shows the evolution of in-plane stresses in the coatings subjected to the two different last thermal cycles. For ease of presentation and comparison, we have selected three planes in the coating, namely, the TBC outer surface, the midpoint (halfway through its thickness) and at the TBC/TGO interface. The heating and holding segments are identical, as expected since they were the same for all the samples with the differences occurring during cooling. During the initial part of heating, the temperature at the top surface of the TBC increases much faster than the coating interior, leading to a differential expansion of the coating, depending on the location. This difference leads to the generation of a compressive stress on the coating surface since the hotter surface is constrained by the cooler, inner parts of the coating and alloy. As the heating continues and heat diffuses in from the surface, the temperatures in the coating interior and in the underlying metallic substrate increase so that the compressive stress at the surface decreases. In contrast, the coating near the TBC/TGO interface is subjected to tensile stress almost immediately, which continues to increase throughout the heating portion of the cycle. Once the maximum temperature is reached and during high-temperature hold, the stresses in the coating are relaxed by creep deformation. By the end of the 4 min hold, the coating is almost stress-free except for near its interface with the metallic bond-coat alloy.

During the earliest part of the cooling, once the heating flame is removed the temperature of the TBC surface drops abruptly as shown in the temperature data in Fig. 3. More striking is the sudden change in the temperature difference between the coating outer surface and the midpoint temperature in the alloy. At the end



**Fig. 6 Optical micrograph of the coatings after planarizing: (a) in the as-sprayed condition, (b) after thermal cycling with only backside cooling, and (c) after thermal cycling with back and front-side cooling on the last cycle**



**Fig. 7 Evolution of stresses in the coating and the temperature difference between TBC surface and TBC/TGO interface calculated by finite element analysis for the two cooling scenarios: (a) with only back-side cooling and (b) with back and front sides cooling**

of the high-temperature hold, the temperature difference between the outer surface and the TBC/TGO interface was 304°C. During the first two seconds of the cooling, this temperature difference dropped to 23°C in the case of coating cooled from the backside only and to -208°C, meaning that the top surface of the coating was 208°C cooler than the metal, when forced cooled from both sides. Such temperature drops lead to the generation of significant tensile in-plane stress at the coating surface: 206 MPa and 375 MPa in the coating cooled only from the back side and in the coating cooled from both sides, respectively. During subsequent cooling, the tensile stress in the coating decreases and then becomes compressive due to the higher thermal expansion of the thick metal substrate. Similar results have also been reported elsewhere [16,27].

### 4.3 Residual Stress Measurement by Raman Spectroscopy

**4.3.1 Stress-Free Raman Peak Shift in Yttria-Stabilized Zirconia With Aging.** The position and width (full width at half maximum) of the Raman peak at around 465  $\text{cm}^{-1}$  after aging the scraped powders at various temperatures are shown in Fig. 8. With aging at higher temperatures, the Raman peak shifted to a lower wavenumber and the peak underwent significant sharpening. The sharpening of Raman bands has been observed previously in yttria-stabilized zirconia coating deposited by electron beam physical vapor deposition process [15] and has been attributed to decreasing anion disorder upon aging and phase evolution. Recently, we have also shown that the sharpening and peak shift of the Raman bands occurs in metastable tetragonal-zirconia powders and coatings with various compositions and microstructure [28]. The shifts shown in Fig. 8 are commensurate with these complementary measurements.

**4.3.2 Raman Peak Shift and Strain Distribution in Thermal Barrier Coatings With Different Cooling Scenarios.** The frequency of the Raman band at 465  $\text{cm}^{-1}$  measured at various locations within the coatings for the two cooling scenarios are shown in Fig. 9. Two specimens with back-side forced cooling only (Fig. 9(a)) and one specimen with back and front-side forced cooling (Fig. 9(b)) were examined. Also plotted in Fig. 9 is the temperature-dependent strain-free peak position determined from the calculated temperatures and the strain-free Raman data from the aging calibration shown in Fig. 8. This has been converted to position-dependent peak position using the calculated temperature

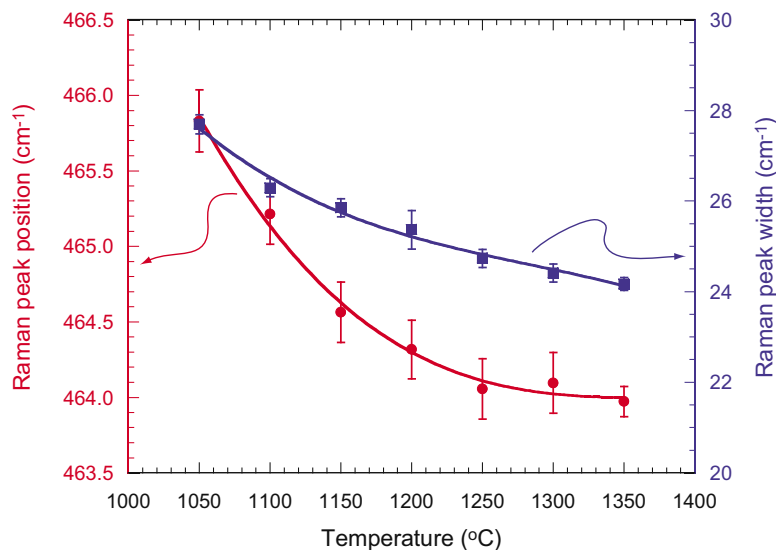


**Fig. 8 Strain-free position and width of the Raman peak around 465  $\text{cm}^{-1}$  of a fragment of APS TBC annealed for 27 h at the various temperatures indicated**

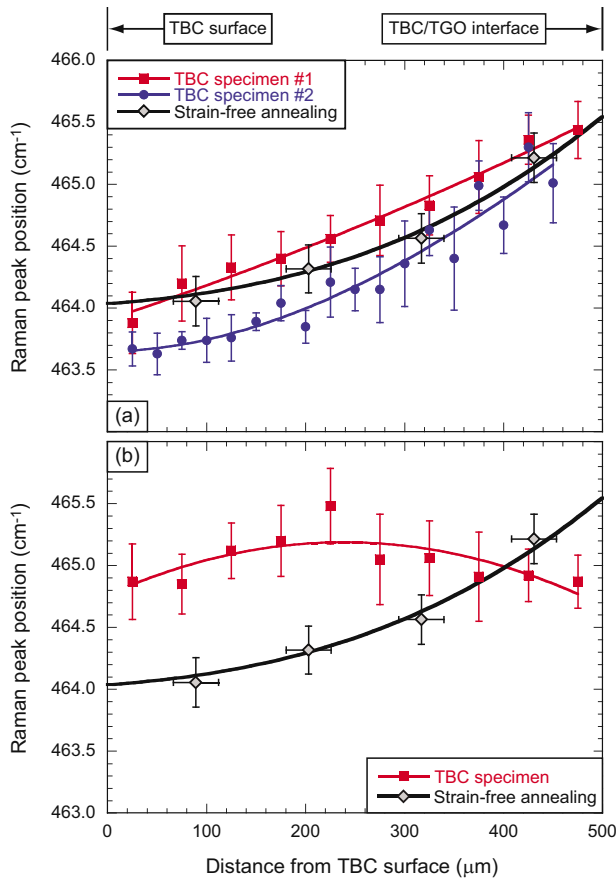


**Fig. 9 Raman peak shift at different location within the coating subjected to cyclic thermal gradient (a) with back-side cooling only and (b) with front-side cooling on the last cycle. The strain-free peak positions at different locations were calculated by combining the temperature-dependent peak position (shown in Fig. 6) and temperature distribution calculated using finite element analysis.**

profile from finite element analysis. In the specimens forced cooled only from the backside, the Raman peak near the surface of the coating has shifted to a lower wavenumber ( $\sim 463.8 \text{ cm}^{-1}$ ) compared with that near the TBC/TGO interface ( $\sim 465.3 \text{ cm}^{-1}$ ). Nevertheless, the two specimens evaluated in this study indicated that the peak shift is rather close to that without any stress. One specimen showed a lower wavenumber than the strain-free annealing (indicating tensile residual stress) and the other showed a higher wavenumber (compressive residual stress). In contrast, the frequencies of the Raman peaks recorded from different depths in the coating force cooled from both sides in the last cycle shifted to a higher wavenumber in most locations, indicating that the residual stress in that coating is mainly compressive. From this data, the calculated strain distributions in the coatings are shown in Fig. 10 after correcting for the frequency shift due to aging. These indicate that the strains in the coatings cooled only from the backside are rather low and almost strain-free, generally, within  $5 \times 10^{-4}$  of being strain-free. One coating showed a slight tensile net strain throughout while the other was slightly compressive except right at the outer surface. The strains in the coating force cooled from both sides, however, are compressive throughout almost the entire thickness switching to tensile strain adjacent to the TBC/TGO interface.

**4.4 Comparison Between Measured and Calculated Stress Distributions.** Although the Raman frequency shifts are measures of strains, it is more convenient and conventional to compare the Raman measurements with the finite element analyses in term of

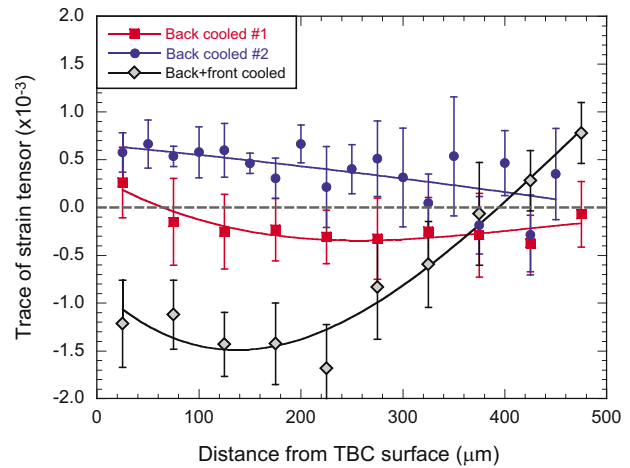


**Fig. 10 Strain distribution through the coating thickness calculated from the measured Raman peak shift. The lines are for visual guide.**

in-plane stress. However, the conversion of Raman peak frequency shifts measured on a cross section to the in-plane stress in an intact coating prior to sectioning involves several assumptions and uncertainties. Typically, it is assumed that the coating is significantly thinner than the metal substrate and all interfaces are considered flat so that the normal stress to the coating surface is zero. This assumption leads to the coating being under biaxial stress  $\sigma_B$ . Cutting the specimen to produce a cross section introduces a new surface that is traction-free and so the stress component normal to the cutting plane, which was a component of the biaxial stress state, now becomes zero at the surface and builds up again going into the coating below the sectioned plane. The biaxial stress  $\sigma_B$  in the coating prior to sectioning can be calculated from the Raman peak shift  $\Delta\nu$  as follows:

$$\sigma_B = \frac{1 - \nu_n}{\Pi} \frac{E_{\text{TBC}}}{E_{\text{dense}}} \Delta\nu \quad (4)$$

where  $\nu_n$  is the Poisson's ratio,  $E_{\text{TBC}}/E_{\text{dense}}$  is the ratio between elastic modulus of the coating and that of dense material.  $\Pi$  is the piezospectroscopic constant of the dense material obtained under uniaxial stress.

Figure 11 shows the stresses calculated using finite element analysis and those obtained from Raman piezospectroscopy based on the above assumption. The calculated stresses at high temperature refer to those generated during instantaneous cooling of the TBC top surface before the entire coating/metal system cools down to room temperature. The sudden cooling of the TBC surface leads to a stress gradient in the coating where the coating surface is subjected to tensile stresses. Assuming a linear fit to the stress profiles in Fig. 11, the stress gradients in the coatings predicted by finite element analysis are  $-0.18 \text{ MPa}/\mu\text{m}$  and  $-0.48 \text{ MPa}/\mu\text{m}$  for the coating cooled from the backside and from both sides, respectively. During subsequent cooling to room temperature, the contraction of the underlying superalloys dominates and the stresses become compressive. In the coatings cooled only from the back side, the measured stresses near the TBC surface were about 20–40 MPa but the average stress in the interior of the coatings were essentially zero. The measured residual stress in the coating cooled from both sides is mainly compressive with a maximum of approximately  $-0.100 \text{ MPa}$ . The stress is slightly tensile near the TBC/TGO interface.

## 5 Discussion

The observations described in this work indicate the cooling conditions applied to a thermal barrier coated system when subjected to thermal cycling under a temperature gradient can dramati-

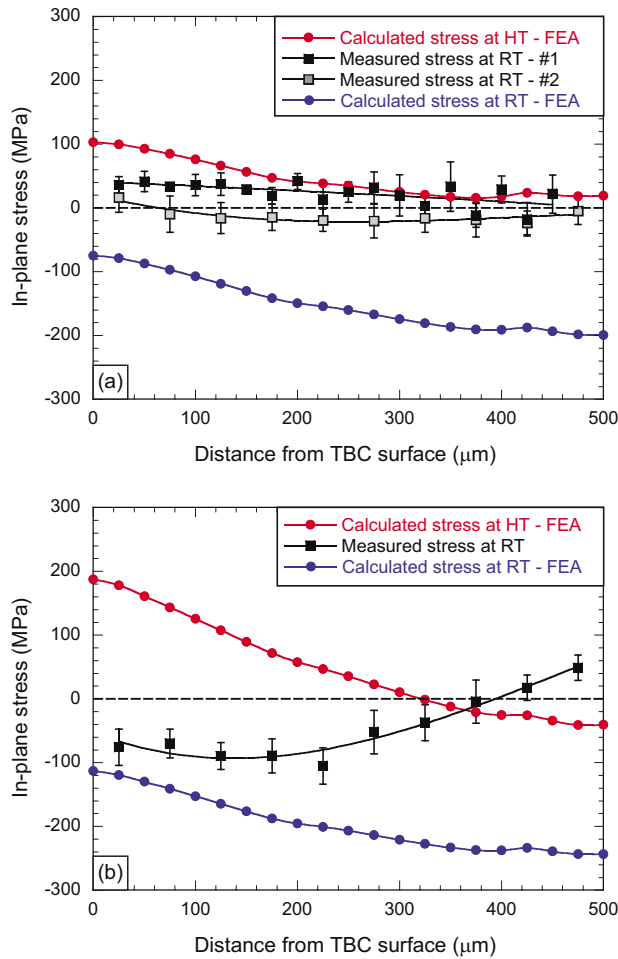


**Fig. 11 Stress distributions in the coating calculated by finite element analysis and measured by Raman spectroscopy (a) for specimens cooled only from the back-side and (b) for specimen cooled from both sides at the last cycle. The calculated stresses at HT represent those immediately after the temperature of the coating surface drops.**

cally affect the stress distribution in the coating. If the surface cooling is sufficiently rapid, cracking can initiate at the surface. In turn, this can modify the residual stress distribution in the coating at room temperature and measured by techniques, such as Raman spectroscopy and X-ray diffraction, which might be used to validate finite element analyses of the stresses. In the following, we discuss the stress evolution in the coatings and its effect on the crack formation. Stress measurement by Raman piezospectroscopy is then revisited to highlight some appropriate considerations that must be taken to obtain reliable measurements.

**5.1 Mechanism of Cracking at the Coating Surface.** As mentioned earlier, the mud-cracking pattern observed in the coating provides direct evidence for the existence of tensile stresses at the coating surface at some stage in the thermal cycling test. The crack spacing  $s$  in the coating can be used to estimate the magnitude of the tensile stress  $\sigma_B$  according to the following relationship [29]:

$$\sigma_B = \left\{ \frac{\Gamma_{TBC} \bar{E}_{TBC}}{1 - \left[ 2 \tanh\left(\frac{s}{2l}\right) - \tanh\left(\frac{s}{l}\right) \right]} \right\}^{0.5} \quad (5)$$

with  $\bar{E}_{TBC} = E_{TBC} / (1 - \nu_{TBC}^2)$  and  $l = (\pi/2)g(D)h$  where  $E_{TBC}$ ,  $\nu_{TBC}$ , and  $\Gamma_{TBC}$  are the elastic modulus, Poisson's ratio, and fracture

toughness of the TBC, respectively.  $h$  is the coating thickness and  $g(D)$  is a parameter dependent on the Dundurs parameter  $D = \bar{E}_{TBC} - \bar{E}_{sub} / \bar{E}_{TBC} + \bar{E}_{sub}$  and plotted in Ref. [29]. For the elastic properties considered in this work, the Dundurs parameter is equal to  $-0.5$  so that  $g(D) \cong 1$  [29]. The fracture toughness of the air plasma spray (APS) TBC is approximately  $30 \text{ Jm}^{-2}$  [30]. Equation (5) predicts a tensile stress in the range of 189–499 MPa for the coating cooled only from the back side with a crack spacing of approximately  $250\text{--}500 \mu\text{m}$ , and a tensile stress of 499 MPa up to 1097 MPa for the coating cooled from both sides (with a crack spacing of  $150\text{--}250 \mu\text{m}$ ). It is worth noting that the cracks observed in the coating include the intrinsic cracks (formed during the plasma spray deposition) as well as those accumulated during the 400 thermal cycles. Thus, the calculated tensile stress is an over estimate and represents the upper limit of the tensile stress in the coating.

Finite element analysis showed that the coating surface exhibited a large in-plane tensile stress during the initial cooling transient as the temperature of the surface dropped due to the sudden cooling and before the coated-superalloy cools down to room temperature (Fig. 7). The tensile stress was generated because of the differential contraction between the coating surface and the coating interior (and the underlying metal). The coating cooled from both sides experienced a temperature drop of  $512^\circ\text{C}$  while the surface temperature of the coating cooled only from the backside dropped by  $281^\circ\text{C}$ . In the elastic regime, the magnitude of the stress is proportional to the temperature drop  $\Delta T$  [7].

$$\sigma_B = \frac{E_{TBC} \alpha_{TBC} \Delta T}{1 - \nu_{TBC}} \quad (6)$$

where  $\alpha_{TBC}$  is the thermal expansion coefficient of the coating. The calculated stresses associated with this sudden cooling were 206 MPa for the coating cooled only from the backside and 375 MPa for the coating cooled from both sides. The reasonable agreement, at least qualitatively, between the stresses estimated from the average crack spacing and those calculated by finite element analysis suggests that the coating surface cracks during the transient cooling period. On further cooling to room temperature, finite element analysis shows that the continued contraction of the underlying metallic substrate puts the coatings, in both cases, under compression.

**5.2 Limitation of the Finite Element Analysis.** Raman measurement indicated that the measured stresses in the coating are smaller than those predicted by finite element analysis. In both cases, finite element analysis suggested that the residual stresses in the coatings are compressive. However, while the experimental measurement showed that the stresses in the coating cooled from both sides were compressive, the measured stress in the coating cooled only from backside was essentially zero. To understand this discrepancy, we have outlined the limitations of the finite element modeling performed in this study.

The first assumption made in this study was that the coating was homogeneous and the effect of the vertical cracks observed in the coating microstructure was not taken into consideration. The formation and propagation of these vertical cracks have two major consequences that were not considered in the present finite element analysis. First, cracking releases some of the stress in the coating. Hence, it is reasonable to expect that the measured stresses are lower than the predicted values. Second, cracking also alters the elastic modulus of the coating. As the cracks initiated from the coating surface and propagated toward the interface due to the in-plane tensile stress, the elastic modulus of the coating is no longer constant. Rather, the elastic modulus would be dependent on the location within the coating because of the presence of surface cracks.

The effect of sintering has also been neglected in the finite element analysis, largely because very little is known about its constitutive behavior. Sintering is a temperature-dependent pro-

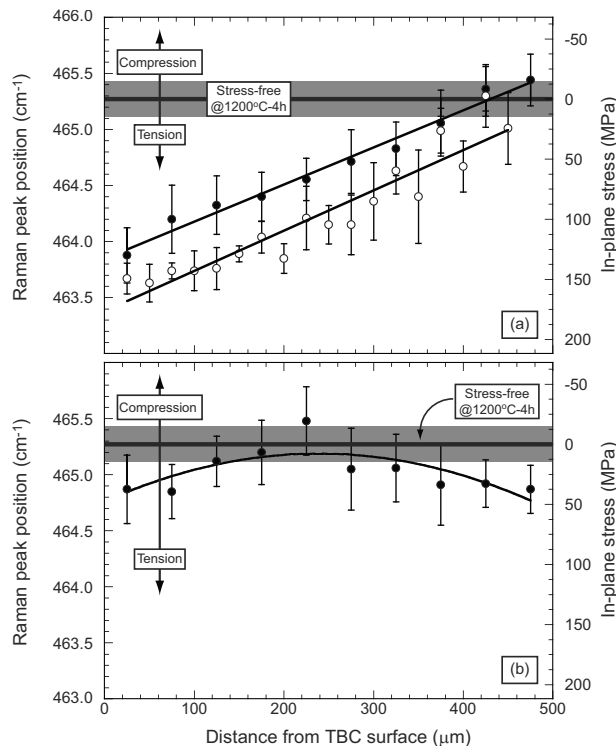


**Fig. 12** Apparent residual stress distribution measured by Raman spectroscopy when a constant stress-free Raman peak shift is used in the calculation: (a) for specimens cooled only from the back side and (b) for specimen cooled from both sides at the last cycle

cess and, hence, is position-dependent in a thermal gradient condition: Sintering occurs at a higher rate at the surface compared with sintering near the TBC/TGO interface. Sintering of the coating increases the thermal conductivity of the coating, redistributes the stress and more importantly, can be expected to increase the elastic modulus of the coating. Here, the elastic modulus of the coating near the surface will be higher than that near the TBC/TGO interface. Such a competition between elastic modulus decrease due to cracking and increase due to sintering is rather complex and beyond the scope of this study.

**5.3 Considerations for Stress Measurement by Raman Piezospectroscopy.** The application of Raman piezospectroscopy to quantify residual stresses in zirconia coatings has been hindered by the difficulty in interpreting the Raman peak shifts and converting them to residual stress. Here, we highlight some crucial considerations in the stress measurement by Raman spectroscopy to ensure the accuracy of the measurement.

The calculation of stress from Raman spectroscopy relies on the accurate determination of the strain-free Raman position. Previously, the stress-free Raman position was considered only to be composition dependent. This study, along with our recent work, however, shows that the peak position also depends on the thermal history of the material (temperature and duration of high-temperature aging). For example, the Raman peak at  $465\text{ cm}^{-1}$  shifts to a lower wavenumber with increasing aging temperature and time [28]. In a thermal barrier coating subjected to a thermal gradient, this leads to the stress-free Raman peak position being dependent on the location within the coating, as shown in Fig. 8. In the coatings investigated in this study, this resulted in a small value for the stress in the coatings. To illustrate the importance of this aging dependence on Raman shift, we also assessed the stresses in the coatings assuming a constant stress-free Raman peak position (Fig. 12). These calculations suggest that the coat-

ings cooled only from the backside exhibited large tensile stresses at the coating surface while the coating near the interface was almost stress-free. In contrast, the coating cooled from both sides appeared to have small tensile stress throughout the coating. Such assessments are quite different from the stress calculation using the corrected temperature-dependent stress-free Raman shift. Furthermore, without this correction the calculated tensile stress throughout the entire coating is inconsistent with the finite element analysis, as well as intuition, which shows that the coating will go into compression at room temperature due to the contraction of the more massive, underlying metal. A similar correction to account for phase partitioning should also be made in quantifying the residual stresses by X-ray diffraction.

## 6 Conclusion

The residual stress in plasma-sprayed zirconia thermal barrier coatings subjected to cyclic thermal gradient has been evaluated using finite element analysis and Raman piezospectroscopy. Microstructural observation revealed that the coating exhibited mud-cracking with the crack spacing controlled by the cooling rate of the coating. Finite element simulation showed that the temperature of the coating surface dropped rapidly, leading to large in-plane tensile stresses at the surface. The magnitude of the stress depends on the cooling rate during thermal cycling: coatings cooled from both sides experienced larger temperature drops and, hence, larger tensile stress than coatings cooled only from the back side. As a result, the crack density is higher in the coating cooled from both sides. Due to cracking, the residual stresses measured by Raman spectroscopy were low, in the order of  $-20\text{ MPa}$  up to  $40\text{ MPa}$  in the coatings cooled only from the back side and  $-100\text{ MPa}$  up to  $50\text{ MPa}$  in the coating cooled from both side at the last cycle of the thermal cycling.

We have also shown that the stress-free Raman peak position, which is crucial in the stress determination, evolves with high-temperature aging. In particular, the position of Raman peak at  $465\text{ cm}^{-1}$  shifts to a lower wavenumber when the coating is aged at a higher temperature. This is crucial when the coating is subjected to prolonged thermal gradient exposure as the stress-free Raman position depends on the location within the coating. Failure to recognize this stress-free peak shift results in erroneous values and, as shown in this work, may lead to incorrect conclusions regarding the stress distribution in coatings subject to exposure in a thermal gradient.

## Acknowledgment

This work is supported by the Office of Naval Research, Contract No. N00014-09-1068. The authors are grateful for fruitful discussion with the late Prof. A.G. Evans (UCSB) and Prof. J.W. Hutchinson (Harvard University).

## References

- [1] Clarke, D. R., and Levi, C. G., 2003, "Materials Designs for the Next Generation Thermal Barrier Coatings," *Annu. Rev. Mater. Res.*, **33**, pp. 383–417.
- [2] Levi, C. G., 2004, "Emerging Materials and Processes for Thermal Barrier Systems," *Curr. Opin. Solid State Mater. Sci.*, **8**, pp. 77–91.
- [3] Evans, A. G., Mumm, D. R., Hutchinson, J. W., Meier, G. H., and Pettit, F. S., 2001, "Mechanisms Controlling the Durability of Thermal Barrier Coatings," *Prog. Mater. Sci.*, **46**, pp. 505–553.
- [4] Christensen, R. J., Lipkin, D. M., Clarke, D. R., and Murphy, K. S., 1996, "Nondestructive Evaluation of the Oxidation Stresses Through Thermal Barrier Coatings Using  $\text{Cr}^{3+}$  Piezospectroscopy," *Appl. Phys. Lett.*, **69**, pp. 3754–3756.
- [5] Paton, N. E., Murphy, K. S., and Clarke, D. R., 2000, "Thermal Barrier Coating Stress Measurement," U.S. Patent No. 6,072,568.
- [6] Gell, M., Sridharan, S., Wen, M., and Jordan, E. H., 2004, "Photoluminescence Piezospectroscopy: A Multi-Purpose Quality Control and Ndi Technique for Thermal Barrier Coatings," *Int. J. Appl. Ceram. Technol.*, **1**(4), pp. 316–329.
- [7] Evans, A. G., and Hutchinson, J. W., 2007, "The Mechanics of Coating Delamination in Thermal Gradients," *Surf. Coat. Technol.*, **201**, pp. 7905–7916.
- [8] Scardi, P., Leoni, M., and Bertamini, L., 1995, "Influence of Phase Stability on the Residual Stress in Partially Stabilized Zirconia TBC Produced by Plasma

- Spray," *Surf. Coat. Technol.*, **76–77**, pp. 106–112.
- [9] Levit, M., Grimberg, I., and Weiss, B.-Z., 1996, "Residual Stresses in Ceramic Plasma-Sprayed Thermal Barrier Coatings: Measurement and Calculation," *Mater. Sci. Eng., A*, **206**, pp. 30–38.
- [10] Kesler, O., Matejcek, J., Sampath, S., Suresh, S., Gnaeupel-Herold, T., Brand, P. C., and Prask, H. J., 1998, "Measurement of Residual Stress in Plasma-Sprayed Metallic, Ceramic and Composite Coatings," *Mater. Sci. Eng., A*, **257**, pp. 215–224.
- [11] Matejcek, J., Sampath, S., Brand, P. C., and Prask, H. J., 1999, "Quenching, Thermal and Residual Stress in Plasma Sprayed Deposits: NiCrAlY and YSZ Coatings," *Acta Mater.*, **47**, pp. 607–617.
- [12] Hobbs, M. K., and Reiter, H., 1988, "Residual Stresses in ZrO<sub>2</sub>-8%Y<sub>2</sub>O<sub>3</sub> Plasma-Sprayed Thermal Barrier Coating," *Surf. Coat. Technol.*, **34**, pp. 33–42.
- [13] Teixeira, V., Andritschky, M., Fischer, W., Buchkremer, H. P., and Stover, D., 1999, "Analysis of Residual Stresses in Thermal Barrier Coatings," *J. Mater. Process. Technol.*, **92–93**, pp. 209–216.
- [14] Greving, D. J., Rybicki, E. F., and Shadley, J. R., 1994, "Through-Thickness Residual Stress Evaluations for Several Industrial Thermal Spray Coatings Using a Modified Layer-Removal Method," *J. Therm. Spray Technol.*, **3**, pp. 379–388.
- [15] Lugh, V., and Clarke, D. R., 2005, "Transformation of Electron-Beam Physical Vapor-Deposited 8 wt % Yttria-Stabilized Zirconia Thermal Barrier Coatings," *J. Am. Ceram. Soc.*, **88**, pp. 2552–2558.
- [16] Traeger, F., Vassen, R., Rauwald, K., and Stover, D., 2003, "Thermal Cycling Setup for Testing Thermal Barrier Coatings," *Adv. Eng. Mater.*, **5**, pp. 429–432.
- [17] Portinha, A., Teixeira, V., Carneiro, J., Beghi, M. G., Bottani, C. E., Franco, N., Vassen, R., Stover, D., and Sequeira, A. D., 2004, "Residual Stresses and Elastic Modulus of Thermal Barrier Coatings Graded in Porosity," *Surf. Coat. Technol.*, **188–189**, pp. 120–128.
- [18] Tomimatsu, T., Kagawa, Y., and Zhu, S. J., 2003, "Residual Stress Distribution in Electron Beam-Physical Vapor Deposited ZrO<sub>2</sub> Thermal Barrier Coating Layer by Raman Spectroscopy," *Metall. Mater. Trans. A*, **34**, pp. 1739–1741.
- [19] Tanaka, M., Hasegawa, M., Dericoglu, A. F., and Kagawa, Y., 2006, "Measurement of Residual Stress in Air Plasma-Sprayed Y<sub>2</sub>O<sub>3</sub>-ZrO<sub>2</sub> Thermal Barrier Coating System Using Micro-Raman Spectroscopy," *Mater. Sci. Eng., A*, **419**, pp. 262–268.
- [20] Limarga, A. M., and Clarke, D. R., 2007, "Piezo-Spectroscopic Coefficients of Tetragonal-Prime Yttria-Stabilized Zirconia," *J. Am. Ceram. Soc.*, **90**, pp. 1272–1275.
- [21] Ahrens, M., Lampenscherf, S., Vassen, R., and Stover, D., 2004, "Sintering and Creep Processes in Plasma-Sprayed TBCs," *J. Therm. Spray Technol.*, **13**, pp. 432–442.
- [22] Schwarzer, J., and Vohringer, O., 2003, "High Temperature Deformation Behavior of the Bondcoat Alloy PWA 1370," *Adv. Eng. Mater.*, **5**, pp. 490–493.
- [23] Brindley, W. J., and Whittenberger, J. D., 1993, "Stress Relaxation of Low Pressure Plasma-Sprayed Nicraly Alloys," *Mater. Sci. Eng., A*, **163**, pp. 33–41.
- [24] Demasi, J. T., Sheffler, K. D., and Ortiz, M., 1989, "Thermal Barrier Coating Life Prediction Model Development," NASA, Technical Report No. 182230, Cleveland, OH.
- [25] Bednarz, P., 2006, "Finite Element Simulation of Stress Evolution in Thermal Barrier Coating Systems," Ph.D. thesis, Forschungszentrum Julich GmbH, Julich.
- [26] Busso, E. P., Qian, Z. Q., Taylor, M. P., and Evans, H. E., 2009, "The Influence of Bondcoat and Topcoat Mechanical Properties on Stress Development in Thermal Barrier Coating Systems," *Acta Mater.*, **57**, pp. 2349–2361.
- [27] Vaßen, R., Kerkhoff, G., and Stover, D., 2001, "Development of Micromechanical Life Prediction Model for Plasma Sprayed Thermal Barrier Coatings," *Mater. Sci. Eng., A*, **303**, pp. 100–109.
- [28] Limarga, A. M., Iveland, J., Gentleman, M. M., Lipkin, D. M., and Clarke, D. R., unpublished.
- [29] Xia, Z. C., and Hutchinson, J. W., 2000, "Crack Patterns in Thin Films," *J. Mech. Phys. Solids*, **48**, pp. 1107–1131.
- [30] Kramer, S., Faulhaber, S., Chambers, M., Clarke, D. R., Levi, C. G., Hutchinson, J. W., and Evans, A. G., 2008, "Mechanisms of Cracking and Delamination Within Thick Thermal Barrier Systems in Aero-Engines Subject to Calcium-Magnesium-Alumino-Silicate (CMAS) Penetration," *Mater. Sci. Eng., A*, **490**, pp. 26–35.